ELECTROCHEMISTRY

High-voltage electrosynthesis of organic-inorganic hybrid with ultrahigh fluorine content toward fast Li-ion transport

Gongxun Lu[1,2]†, Qiangqiang Qiao[1]†, Mengtian Zhang[2]†, Jinsen Zhang[1], Shuai Li[1], Chengbin Jin[3], Huadong Yuan[1], Zhijin Ju[1], Rong Huang[4], Yujing Liu[1], Jianmin Luo[1], Yao Wang[1]*, Guangmin Zhou[2]*, Xinyong Tao[1]*, Jianwei Nai[1]*

Hybrid materials with a rational organic-inorganic configuration can offer multifunctionality and superior properties. This principle is crucial but challenging to be applied in designing the solid electrolyte interphase (SEI) on lithium metal anodes (LMAs), as it substantially affects Li$^+$ transport from the electrolyte to the anode. Here, an artificial SEI with an ultrahigh fluorine content (as high as 70.12 wt %) can be successfully constructed on the LMA using a high-voltage electrosynthesis strategy. This SEI consists of ultrafine lithium fluoride nanocrystals embedded in a fluorinated organic matrix, exhibiting excellent passivation and mechanical strength. Notably, the organic-inorganic interface demonstrates a high dielectric constant that enables fast Li$^+$ transport throughout the SEI. Consequently, LMA coated with this SEI substantially enhances the cyclability of both half-cells and full cells, even under rigorous conditions. This work demonstrates the potential of rationally designed hybrid materials via a unique electrosynthetic approach for advanced electrochemical systems.

INTRODUCTION

The combination of organic and inorganic components at the nanoscale into a single material has opened up a new area for hybrid materials, whose multifunctional traits enable them applicable in a variety of fields, including optics, electronics, mechanics, catalysis, energy, and biology (1–3). In general, the organic components in hybrid materials provide good structural flexibility, tunable electronic properties, and low density, while the inorganic ones contribute to outstanding electrical resistivity, high thermal stability, good mechanical strength, and chemical stability (4, 5). In addition to integrating distinct characteristics, the hybrid interface between the two components likewise allows for improved or even new properties, particularly for mass transport (6, 7). A noteworthy demonstration is the organic-inorganic hybrids applied in solar cells (2, 8). It is found that the introduction of some organic species could effectively passivate the defects on the surface of the inorganic light-absorber framework, leading to an enhanced charge carrier transport efficiency cross through the hybrid interface (9, 10). Furthermore, the hybridized materials can also support fast molecular transport and electronic conduction that governs electrocatalysis, biosensors, and nanofluidics (11, 12).

In an electrochemical system regarding lithium metal batteries, which are widely considered the next generation of energy storage devices, an ineluctable but important organic-inorganic material is the solid electrolyte interphase (SEI) layer that commonly exists on the surface of the lithium metal anode (LMA). The SEI layer is usually generated from chemical/electrochemical reactions between the electrolyte and the lithium metal, forming a hybrid structure of inorganic nanoparticles embedded within an organic matrix (13). It is well accepted that the Li ions (Li$^+$) prefer to transport via the organic-inorganic interface rather than within either individual component (14–16). Therefore, the structural configuration of the organic-inorganic interface within the SEI layer, including the constituent, amount, and distribution of the organic/inorganic components, dictates the Li$^+$ transport properties (for example, the conductivity and homogeneousness) from the electrolyte toward the anode and thus substantially affect the electrochemical performance of the LMA. In a conventional electrolyte-derived SEI, oxygen-based components, such as inorganic Li$_2$O nanoparticles and oxygen-contained organic matrix (OOM), are usually dominated. However, such SEIs fail to satisfy a desired Li$^+$ transport, leading to an uneven Li deposition on the LMA. As a result, Li dendrites would easily grow and consequently cause performance degradation and safety concerns (17). Recently, enormous researchers have focused on the fluorination of the SEI (18), particularly have made progress in tuning the constituent of the inorganic component, that is to construct LiF-involved artificial SEI to realize better Li deposition behavior (19–21), due to the higher mechanical strength, superior chemical stability, and lower Li$^+$ diffusion barrier of the LiF compared to the Li$_2$O (22). Some strategies have been proven to be effective in generating such LiF-involved SEI, including introducing fluorinated additives [such as LiF microcrystals and fluoroethylene carbonate (FEC)] (23, 24), increasing Li salt concentration (25, 26), or regulating Li salt decomposition (27, 28). Nevertheless, the fluorine content obtained from the current strategies is limited (mostly below 40 wt %). The Li$_2$O is still the main inorganic component of such SEIs, within which the Li$^+$ transport cannot be markedly improved and thus impede the LMA operated in some extreme conditions, for example, in ester-based electrolytes or at low temperatures. On the other hand, the manipulation of the constituent of the organic

components in the SEIs is difficult, making the study of its impact on the Li$^+$ transport rare.

Here, by introducing a distinctive high-voltage electrosynthesis technique, we demonstrate an artificial SEI with ultrahigh fluorine content (above 70 wt %) consisting of ultrafine LiF nanocrystals and fluorine-enriched organic matrix (FOM) can be fabricated on the LMA. Various characterization techniques and multiple theoretical simulations have been used to disclose the formation mechanism of the organic/inorganic components under the high-voltage electric field, the physiochemical characteristics of this artificial SEI layer, and the underlying mechanism that how the constituent, amount, and distribution of those components affect the Li$^+$ transport behaviors. Meanwhile, we establish a theoretical model based on the dielectric constant to disclose the Li$^+$ transport mechanism across the organic-inorganic interface within the SEI. Last, the electrochemical performance of the LMA protected by the as-synthesized LiF-FOM layer has been evaluated by both half-cell using ether/ester-based electrolytes even at large current density, and full cell using ester-based electrolytes even under rigorous working conditions, such as lean electrolyte, low ratio of negative/positive electrode capacity (N/P ratio), and low temperature.

RESULTS

Electrosynthesis of the LiF-FOM layer

The preparation of the LiF-FOM is based on an electrolysis process, and the detailed process is shown in Fig. 1A. In the electrolytic cell, bare Li metal (B-Li) foil is used as both the cathode and the anode, while the pure FEC without any lithium salt additive is used as the electrolyte. Under a high voltage (600 V), the anodic Li^0 will be oxidized to Li$^+$, solvated with the FEC molecules, and dissolved into the solution, which is confirmed by the changes in the surface morphology of the anodic Li foil (fig. S1) and the color of the electrolyte solution before and after the electrolysis (fig. S2). An emerging peak at −0.1 parts per million (ppm) in ^{7}Li nuclear magnetic resonance (NMR) (Fig. 1B) and a slight blueshift in Raman spectra (fig. S3) of the electrolyte solution after the electrolysis confirm the solvation of the Li$^+$ with the FEC molecules (29, 30). In addition, no obvious change is found in Fourier transform infrared (FTIR) and ^{13}C NMR spectra of the electrolyte solution before and after the electrolysis (fig. S4), excluding the generation of some other new substance during the electrolysis process.

It should be noted that the peak in the ^{19}F NMR spectrum displays an unexpected upfield shift after the electrolysis (Fig. 1C), which is opposite to those reported cases in which FEC works as a
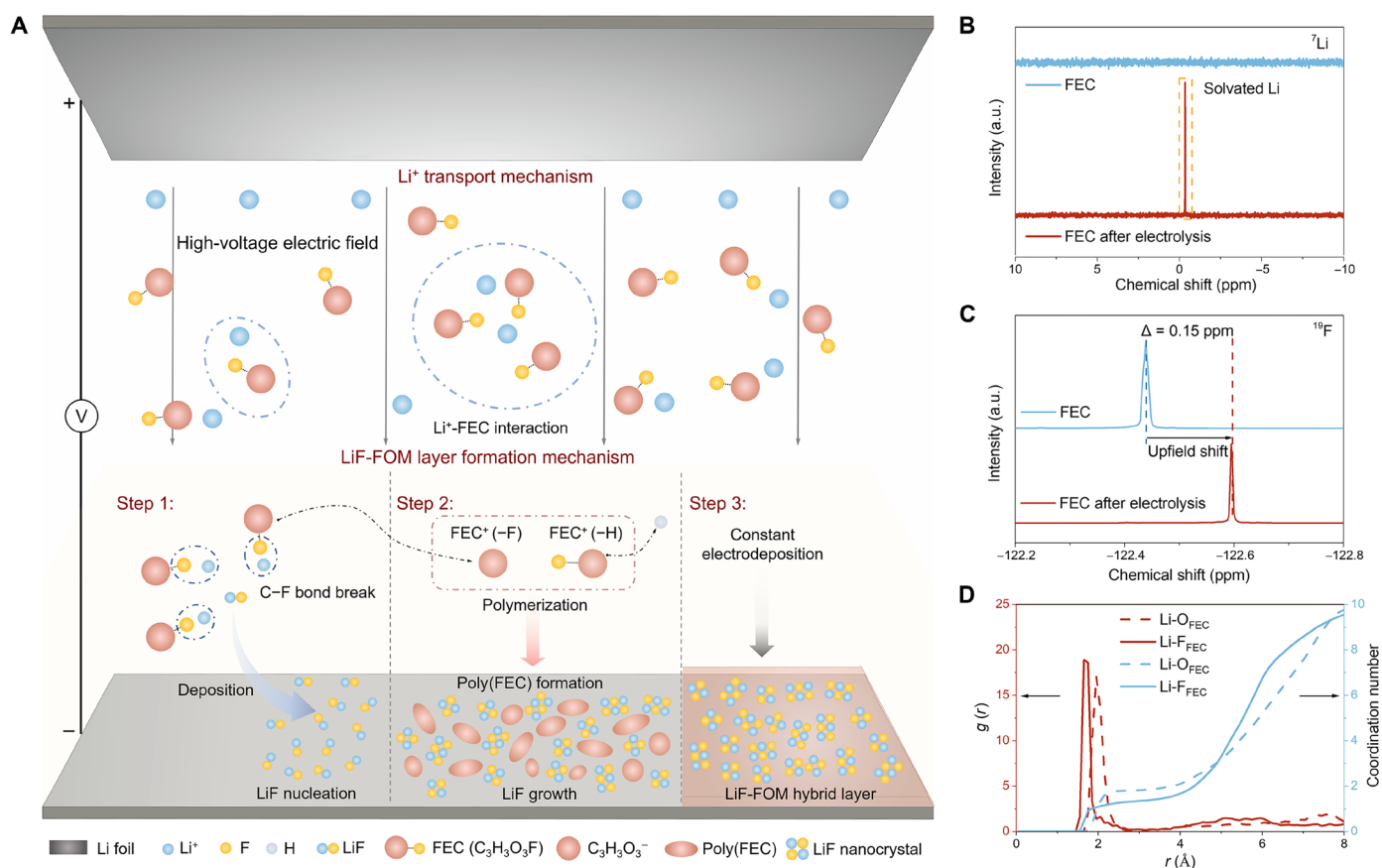

Fig. 1. High-voltage electrosynthesis process of the LiF-FOM layer. (**A**) Schematic illustration of the construction of the LiF-FOM on the surface of LMA under a high-voltage electric field. (**B**) The ^{7}Li nuclear magnetic resonance (NMR) spectra of FEC electrolytes before and after the electrolysis process. (**C**) The ^{19}F NMR spectra of FEC electrolytes before and after the electrolysis process. (**D**) Radial distribution function of Li-O and Li-F interaction and relationship between the coordination number and bond distances under the C—F bond elongated system. a.u., arbitrary units.

common electrolyte additive and the O atom from the C=O bond in the FEC molecule direct the interaction with the Li^+ ions (*31*, *32*). The ab initio molecular dynamics (AIMD) simulations confirm that the Li-O interaction dominates the first coordination shell of Li^+ to form a Li^+-O_4 solvation structure when the FEC serves as the solvent in a common case (fig. S5, A and B). However, in our case, the FEC molecules are subjected to a high-voltage electric field. Consequently, the C—F bond in FEC tends to become polarized and elongated, shifting from a covalent to a more electrostatic character (*33*, *34*). This change imparts the fluorine atom with a larger dipole moment, potentially enabling it to directly interact with Li^+. This hypothesis is supported by AIMD findings showing that the fluorine atom in FEC can enter the first coordination shell of Li^+ to form a Li^+-O_2F_2 solvation structure when the C—F bond lengths in FEC are extended (Fig. 1D and fig. S5A). As a result, a special Li^+-(FEC) solvation structure involved with the Li-F interaction rather than just the Li-O interaction emerges. This structure aligns with the ^{19}F NMR spectral observations (Fig. 1C) and is realized by the high-voltage electric field applied in our study. The computational results further show that the lowest unoccupied molecular orbital (LUMO) energy of the Li^+-O_2F_2 solvation structure is notably lower than that of the FEC molecule (fig. S5C), suggesting a preferential electroreduction of the Li^+-O_2F_2 structure compared to free FEC molecules. Moreover, the LUMO energy of the Li^+-O_2F_2 configuration is slightly lower than that of the Li^+-O_4 one, implying that this unique solvation structure would be easier to reduce to form the fluorine-based products than the conventional one. Building on the enhanced electroreduction tendency, the elongated C—F bond in Li^+-(FEC) is predisposed to cleavage during the electrolytic process. The robust Li-F interaction and its pronounced prevalence in the local environment facilitates substantial nucleation of the LiF nanocrystals. Simultaneously, the FEC molecules would undergo a sustained dehydrogenated polymerization process that is realized by the high-voltage electric field (fig. S6) (*35*, *36*). As a result, a unique FOM would be also produced on the surface of the cathodic Li metal, where the as-formed LiF nanocrystals are embedded. Eventually, an organic-inorganic (LiF-FOM) hybrid layer coated on Li metal (denoted as LiF-FOM/Li) can be obtained.

Structure characterizations of the LiF-FOM layer

The LiF-FOM coated on the surface of the Li metal foil is a light-yellow–colored, homogeneous, compact layer (Fig. 2A). The atomic force microscopy (AFM) verified the dense and flat morphology of the LiF-FOM layer (Fig. 2B). Besides, with the formation of the LiF-FOM layer on the Li metal foil, the average Young's modulus increases from 1.5 to 6.4 GPa (Fig. 2C and fig. S7). The higher Young's modulus indicates that the LiF-FOM layer could be more effective in suppressing the potential growth of Li dendrite and withstanding the high stress from the huge volume change during cell cycling (*37*). Upon exposure to the air with a relative humidity of ~30%, the B-Li turned black within an hour (fig. S8). In contrast, the LiF-FOM/Li maintained its color, indicating that the compact LiF-FOM layer can also provide effective hydrophobic protection for the Li metal.

To accurately visualize the sensitive structure of the LiF-FOM at atomic precision, the LiF-FOM was deposited on the surface of the copper mesh under the same electrolytic conditions and observed by the cryo–transmission electron microscopy (cryo-TEM) technique. The scanning TEM (STEM) and associated energy-dispersive x-ray

spectroscopy elementary mapping images verify that the LiF-FOM exhibits dense deposition and uniform distribution of C, O, and F elements, especially containing an ultrahigh percentage of the F element (70.12 wt %) (Fig. 2D and fig. S9). This fluorine content is the highest so far among current reports for the organic-inorganic hybrid SEIs (table S1). In addition, the thickness of the layer was estimated to be within the 1.5- to 2.0-μm range based on the TEM image (Fig. 2E). The high magnification TEM image and the selected area electron diffraction pattern reveal that numerous LiF nanocrystals with an average size of ~3.2 nm are uniformly distributed within the LiF-FOM (Fig. 2, F and G, and fig. S10). As proved by the high-resolution TEM image from the marked yellow rectangular area in Fig. 2G, the calibrated interplanar spacings of 2.32 and 2.01 Å match well with the (111) and (200) plane of crystalline LiF, respectively (Fig. 2H) (*38*). It should be mentioned that the material filled at the gap between the LiF nanocrystals should be the FOM. In the x-ray photoelectron spectroscopy (XPS) spectra, higher concentration of LiF signal and the more discernible peaks of C—O, C=O, COO⁻, and C—F groups can be observed in the F 1s, Li 1s, and O 1s spectra of the LiF-FOM/Li sample than those of the B-Li sample (Fig. 2, I to K, and fig. S11), which proves the existence of the LiF and the FOM. Furthermore, the FTIR characteristic groups (including C=O, C—O—C, C—O, and C—F) of LiF-FOM/Li are similar to the FEC, proving that the organic components are derived from the FEC molecules and exist as an oligomer since an intense polymerization would generally induce some certain FTIR peaks disappearing or new peak emergence (fig. S12) (*39*). The matrix-assisted laser desorption/ionization–time-of-flight mass spectrometry (MALDI-TOF-MS) verifies that the FOM consists of Li^+-(FEC)–contained polymers (fig. S13), which proves that the Li^+-(FEC) structure allows being polymerized under the high-voltage electric field. To investigate the depth distribution of elements in the LiF-FOM, TOF secondary ion mass spectrometry (TOF-SIMS) was performed. The detection of an ultrahigh intensity of fluorine-involved species (e.g., F^-, LiF^-, and LiF_2^-) from the depth profiles (fig. S14) and their distribution images (Fig. 2L) for LiF-FOM/Li indicates that LiF nanocrystals are abundant and homogenously distributed in the protective layer, while the B-Li is mainly composed with high content of carbon- and oxygen-involved species (e.g., C_2^-, O^-, and CH^-) (fig. S15) (*40*). In addition, some representative fragments from the FOM, including the $CHOF^-$, CH_2CHOLi^-, and CF^- species, are also found to be evenly distributed around the LiF nanocrystals. Therefore, the above results confirm that the unique LiF-FOM, an F-dominated protective layer consisting of LiF nanocrystals evenly anchored within an FEC-derived organic matrix, has been successfully created.

Electrochemical performance and structural stability of the LiF-FOM/Li

To verify the impact of LiF-FOM on the electrochemical stability of the LMA, galvanostatic plating/stripping tests in Li symmetric cells using ether-based electrolytes were first carried out. The voltage plateau of the LiF-FOM/Li anode is extremely stable under a controlled Li plating/stripping capacity of 1 mAh cm⁻² at 1 mA cm⁻², even after ultralong-time cycling for over 3600 hours (Fig. 3A). In contrast, the cell with a B-Li anode displays much inferior electrochemical cycling, which shows a gradual increase in the voltage hysteresis and fails within only 800 hours. This can be ascribed to the elevated charge transfer resistance caused by electrical disconnection and
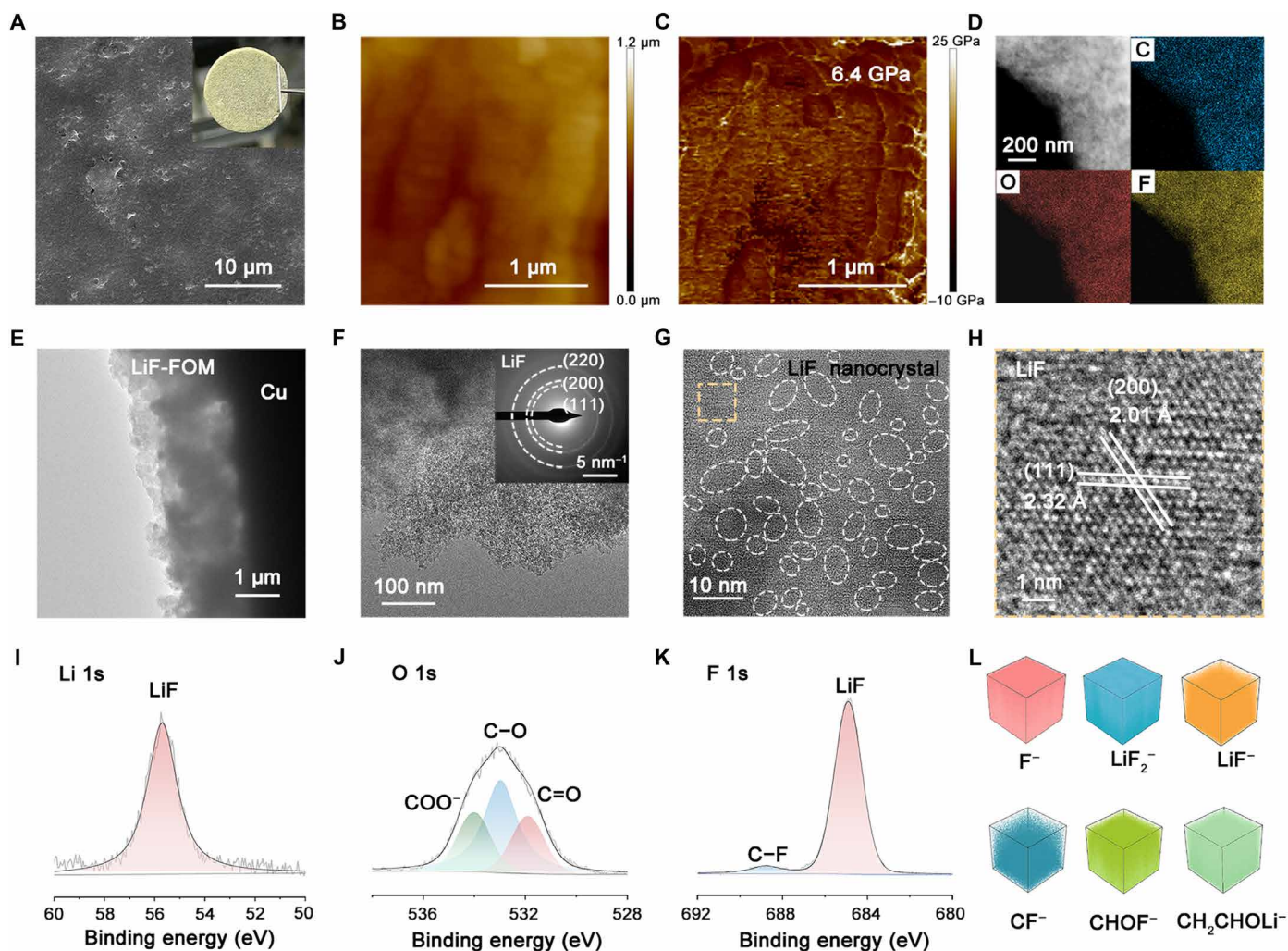
Fig. 2. Structure characterizations of the LiF-FOM layer. (**A**) The top-view scanning electron microscopy image and digital image (inset) of the LiF-FOM. (**B**) Atomic force microscopy topography image of the LiF-FOM. (**C**) The distribution of Young's modulus on the surface of the LiF-FOM/Li. (**D**) The scanning transmission electron microscopy (STEM) image and corresponding energy-dispersive x-ray spectroscopy (EDS) mapping results of the LiF-FOM layer. (**E**) The cryo-TEM image of the LiF-FOM layer at low magnification. (**F**) The cryo-TEM image of the LiF-FOM layer at high magnification and the corresponding selected area electron diffraction patterns (inset). (**G**) The high-resolution TEM (HRTEM) image of the LiF-FOM layer. (**H**) The corresponding HRTEM image of the marked area from (G). X-ray photoelectron spectroscopy (XPS) spectra of the Li 1s (**I**), O 1s (**J**), and F 1s (**K**) of the LiF-FOM/Li. (**L**) The time-of-flight secondary ion mass spectrometry three-dimensional images of the different species for LiF-FOM/Li.

electrolyte depletion because of the repeated growth/corrosion of Li dendrites (*41*). Similar results can be observed at a higher plating/stripping density and capacity of 5 mA cm^{-2} and 5 mAh cm^{-2}, respectively. The LiF-FOM/Li symmetric cell stably cycles for 1200 hours, but the one that uses a B-Li anode displays gradually increasing overpotential after 100 hours (fig. S16). Notably, the LiF-FOM/Li anodes have greater long-term stability than previously reported LMAs shielded by various advanced protective layers using ether-based electrolytes at high current densities and area capacities (fig. S17 and table S2).

The electrochemical kinetics of Li plating/stripping was also evaluated. Tafel plots (Fig. 3B) obtained from the CV curve (fig. S18) and the corresponding exchange current density (j_0) obtained from the intercept demonstrate a higher j_0 for LiF-FOM/Li (0.85 mA cm^{-2}) than that for B-Li (0.39 mA cm^{-2}), signifying a faster Li$^+$ transport through

the LiF-FOM than the regular SEI on the B-Li (*42*). Moreover, the Li$^+$ transference numbers (t_{Li}^+) of the B-Li are measured to be 0.33, while that of the LiF-FOM/Li increases to 0.68 (fig. S19). The enhanced t_{Li}^+ implies a smaller Li$^+$ concentration gradient within the LiF-FOM layer (*43*). To illustrate the underlying mechanism, we further examined the electrochemical impedance spectra (EIS) of the Li symmetric cell with B-Li or LiF-FOM/Li before and after 100 cycles. Lower SEI resistance (R_{SEI}) is obtained for the symmetric cell with LiF-FOM/Li than that with the B-Li before cycling (fig. S20), suggesting that the existence of the LiF-FOM effectively facilitates the Li$^+$ transporting from the electrolyte to the anode. After 100 cycles, the R_{SEI} of LiF-FOM/Li (14.7 ohms) is much smaller than that of B-Li (62.3 ohms), confirming the formation of a highly conductive SEI of LiF-FOM/Li (*44*, *45*). The resistance of charge transfer (R_{ct}) showed a similar result, decreasing from 28.8 to 4.3 ohms with the protection of the LiF-FOM (Fig. 3C).
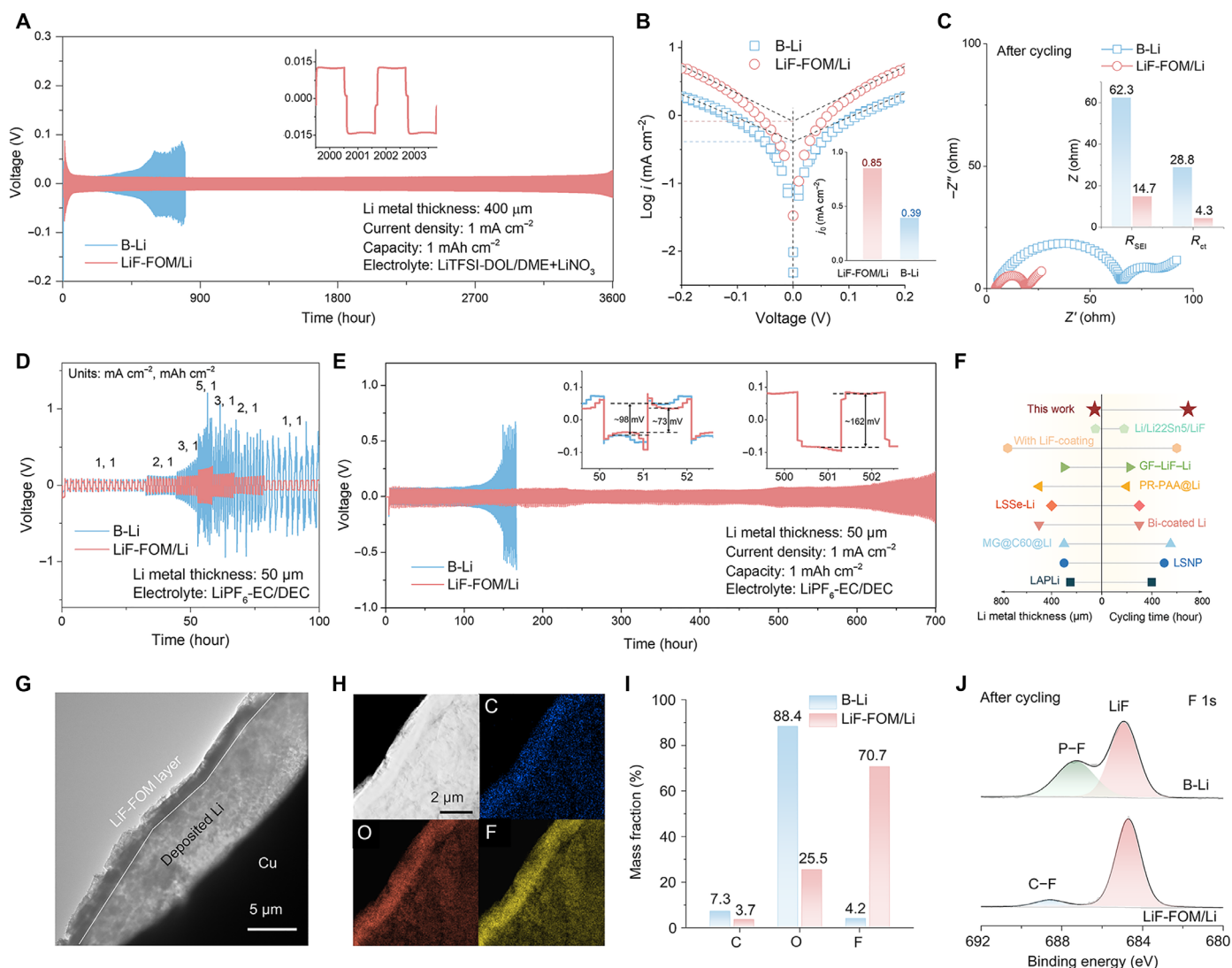
Fig. 3. Electrochemical performance and structural stability of the LiF-FOM/Li. (**A**) Cycling stability of symmetrical cells with B-Li and LiF-FOM/Li using the ether-based electrolyte. The inset is the voltage profile during 1000 cycles. (**B**) Tafel plot and the corresponding exchange current density (inset) of Li symmetrical cells with B-Li and LiF-FOM/Li. (**C**) Nyquist plot of Li symmetrical cells with B-Li and LiF-FOM/Li after 100 cycles. The inset is the obtained R_{SEI} and R_{ct}. (**D**) Rate performance of symmetric cells with B-Li and LiF-FOM/Li using the ester-based electrolyte. (**E**) Cycling stability of symmetrical cells with B-Li and LiF-FOM/Li using the ester-based electrolyte. The insets are the voltage profile during cycles. (**F**) Comparison of the cycling time and Li metal thickness of symmetric cells using ester-based electrolyte with the LMA stabilized by the LiF-FOM layer and other reported diverse artificial SEI layers. (**G**) The cryo-TEM image of the LiF-FOM layer after Li deposition. (**H**) The STEM images and corresponding EDS mapping results of the LiF-FOM layer after Li deposition. (**I**) The relevant mass fraction comparison of varied elements in the SEIs for the B-Li and the LiF-FOM after Li deposition. (**J**) The F 1s XPS spectra of the B-Li and the LiF-FOM/Li after 50 cycles.

The electrochemical measurements were further conducted on electrodes with a thickness restricted to 50 μm and used 1 M $LiPF_6$ in the ester-based electrolyte. The symmetric cell with the LiF-FOM/Li exhibited steady and low Li plating/stripping overpotentials of 95, 141, 220, and 366 mV at various current densities of 1, 2, 3, and 5 mA cm^{-2}, respectively, with fixed Li deposition capacity of 1 mAh cm^{-2}, verifying fast Li$^+$ migration kinetics and superior interface properties (Fig. 3D). In addition, the voltage-time profiles show that the Li symmetric cell with a B-Li anode presents gradually increased overpotentials as time goes by, which reaches 600 mV at the ~150th hour at a current density of 1 mA cm^{-2} with a Li deposition capacity of 1 mAh cm^{-2} (Fig. 3E). On the sharp contrary, the Li symmetric

cell with LiF-FOM/Li exhibits a remarkable cyclability for at least 700 hours with a much smaller overpotential of 73 mV at the ~50th hour and 162 mV at the ~500th hour. In particular, the performance of the LiF-FOM/Li symmetric cell with thinner Li metal in this study is better than those of previously reported Li symmetric cells in ester-based electrolytes (Fig. 3F and Table S3). Furthermore, cycling stability tests with high depth of discharge (DOD) were performed. Notably, thin Li anodes coated with the LiF-FOM layer can stably run over 300 and 400 hours with 40 and 60% DOD, respectively, at 1 mA cm^{-2} (fig. S21). This underscores the LiF-FOM layer's effectiveness in maintaining cycling performance under rigorous cycling conditions.

To reveal the structural stability of the LiF-FOM layer for the LMA, the morphology of the Li plating was first investigated. Without the protection of the LiF-FOM layer, irregular and loose Li dendrites would grow on the B-Li anode even at the first plating (figs. S22, A and B, and S23, A and B). The scanning electron microscopy (SEM) image of the cycled B-Li anode (after 50 cycles) shows a rough and porous layer, where dendritic Li and "dead" Li cover the entire electrode surface (fig. S22, C and D). In contrast, Li metal would manifest a uniform and compact deposition on the LiF-FOM coated LMA at the 1st and even at the 50th plating (Fig. 3, G and H, and fig. S24). It is also observed that the surface of the LiF-FOM layer would exhibit localized cracking in the subsequent cycling process. This phenomenon arises from the existence of a large amount of fragile LiF. Nevertheless, this fracturing is confined to the outer layer, whereas the inner layer of LiF-FOM remains compact and firmly adhered to the LMA (fig. S25). Generally, the morphology of the Li plating is usually determined by the nanostructure and composition of the SEIs. The common SEI on the B-Li anode displays typical oxygen-dominated composites (Fig. 3I and fig. S23C), where the mosaic structure consists of crystalline Li_2O and OOM (fig. S23D) (46, 47). In contrast, the composition of the SEI on the LiF-FOM/Li is fluorine-dominated (Fig. 3I and fig. S26A), which contains a large amount of LiF nanocrystals and FOM even after cycling (figs. S26B and S27). Moreover, Li_2CO_3 and P−F species can be detected by the XPS spectra of the B-Li but not by that of the LiF-FOM/Li after cycling, implying that the potential decomposition of the $LiPF_6$-contained ester electrolyte could be inhibited with the protection of the LiF-FOM layer (Fig. 3J and fig. S28). To demonstrate the superiority of the LiF-FOM layer, we compare the stability of the SEI's structure and the related electrochemical performance of the LMAs coated with the LiF-FOM layer and those coated with a layer derived from conventional FEC-engaged strategies. For example, upon immersing Li metal into FEC solvent for 24 hours, a fluorine-contained layer can be formed on the surface of the Li metal (fig. S29, A and B). Regrettably, this layer fails to persist stability during cycling, whose composition would be gradually transformed to an oxygen-dominated one (with the F content of only ~8.5 wt %) that derived from the electrolyte decomposition after only 50 cycles (fig. S29, C and D). As a result, the symmetrical cell can only be stabilized for up to 200 hours (fig. S29E). Analogously, while adding FEC as an additive in the ester-based electrolytes, the SEI composed of LiF/Li_2O and OOM (with the F content of ~33.7 wt %) after 50 cycles (fig. S30, A to C). In this case, the symmetrical cell can be stabilized for 350 hours (fig. S30D). The above comparison indicates that the high-voltage electrosynthetic technique used in this work can introduce a larger number of fluorine-related species into the SEI, whose structural stability during long-term cycling is also superior to the conventional fluorine-enriched artificial SEIs. Apart from the case in the ester-based electrolytes, the LiF-FOM layer can also demonstrate excellent structural stability in the ether-based electrolytes. The XPS and cryo-TEM data show that the LiF-FOM layer can maintain an impressively high fluorine concentration (above 60 wt %) with a harmonious blend of LiF nanocrystals and fluorine-related organic species even after enduring 500 cycles (figs. S31 and S32).

The working mechanism of the LiF-FOM layer

The above results suggest that the exceptional cycling stability of the LiF-FOM/Li should be due to its unique SEI that is constructed by a fluorinated organic-inorganic hybrid layer. To be specific, the LiF nanocrystals have sufficient grain boundaries for rapid Li^+ transport across the SEI, while the FOM filled among the LiF nanocrystals serves as a flexible conductive constituent to support homogeneous Li^+ diffusion. To better reveal this Li^+ transport mechanism, three different cases of organic-inorganic interphase were established (fig. S33): (i) the Li_2O-OOM representing the most common SEI's structure that usually formed on the B-Li, (ii) the LiF-OOM representing the structure of some reported artificial SEIs that use premade but a limited amount of LiF nanocrystals while the organic component is still oxygen-dominated (47, 48), and (iii) the LiF-FOM representing the unique SEI structure in this work. First, it is found that the Li^+ diffusion barrier on the isolated LiF surface (0.16 eV) is much smaller than that on the isolated Li_2O surface (0.30 eV) (Fig. 4, A to C), which is consistent with previous reports (49). By incorporating the organic component on the inorganic surface, all the Li^+ diffusion processes exhibit lower energy barriers, indicating that the organic-inorganic interface can endow a faster Li^+ transport. In particular, the energy barrier of the LiF-FOM is 0.06 eV, which is much lower than that of the LiF-OOM (0.11 eV) and Li_2O-OOM (0.17 eV) (Fig. 4, A to C). Moreover, the largest diffusion coefficient was found for the LiF-FOM ($7.57 \times 10^{-8}\,m^2\,s^{-1}$), which is superior to those of other organic-inorganic interphases (table S4). According to the above results, it is proposed that the dielectric constant of the organic/inorganic phase is found to strongly influence the Li^+ transport behavior, that is the higher the dielectric constant (table S5), the lower the energy barrier for the Li^+ transport. This might be because the elevated dielectric constant can effectively alter the bonded structure and ion polarization that reduce the Coulombic repulsion (50, 51), thus lowering the migration barrier and boosting ion transport rates (52).

The finite element analysis (FEA) further implies that the dielectric constant of the components might also be able to regulate the potential tip effect of the local electric field induced by some ineluctable protuberances on the LMA. Taking the dielectric constant of the organic component as the variable, under the low numeric value (as low as ~4), the local electric field would be concentrated near those protuberances, which could lead to a subsequent Li^+ deposition preferential in these areas and, in turn, reinforce the tip effect, lastly resulting in a dendrite morphology. In contrast, the component with a high dielectric constant (as high as ~12) could effectively mitigate the uneven local electric field along the protuberances, guiding a uniform Li^+ deposition (Fig. 4D). Quantification analysis shows that the tip electric field intensity would decrease exponentially as the increase of the dielectric constant, the maximum reduction of which can be as high as 64% (Fig. 4E). Concurrently, the alleviated local electric field under the high dielectric constant could contribute to reducing the electric potential difference near the LMA surface (Fig. 4F), which would diminish battery polarization as observed in the experimental results (Fig. 3, A and E) (53). Furthermore, the FEA was also executed to illustrate the correlation between the SEI structure and the Li^+ electrochemical behavior across the SEI. For the B-Li, the Li^+ transport ability crossing the SEI is relatively slower and uneven because of the oxygen-dominated feature of the SEI's composition as well as the inhomogeneous distribution of the components within such SEIs (Fig. 4G). As a result, an uneven Li^+ concentration distribution can be obtained within the SEI and at the interface between the SEI and the LMA (fig. S34). This would further lead to an inhomogeneous local current density (LCD) on the LMA (Fig. 4G).
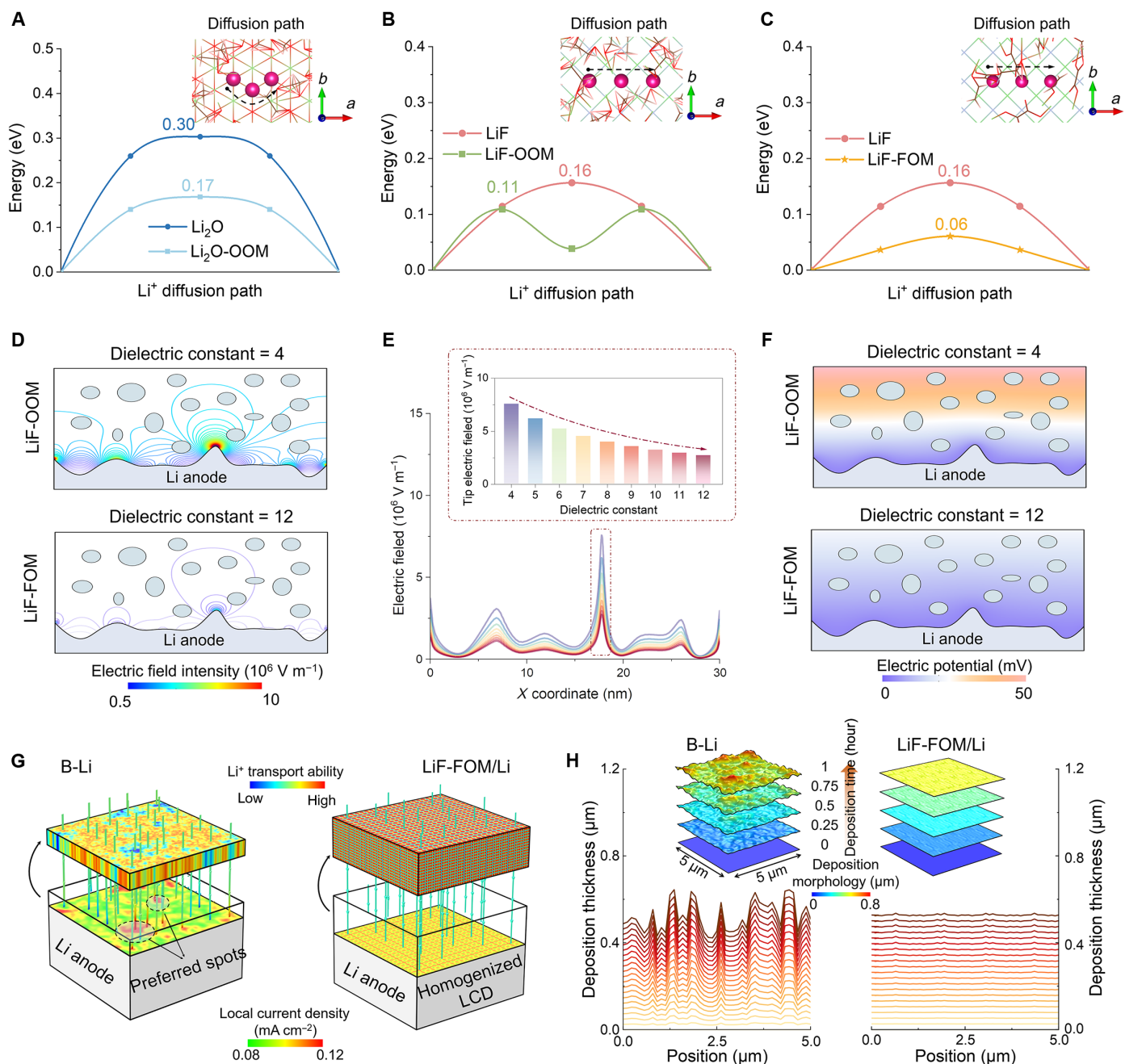
Fig. 4. Simulation of the Li⁺ transport and deposition properties. ($\mathbf{A}$ to $\mathbf{C}$) Diffusion barrier energy of Li⁺ on the isolated Li_2O surface, LiF surface, and their interface with the OOM or FOM. ($\mathbf{D}$) Electric field intensity distribution in SEI under the case of the dielectric constant of the organic phase is 4 or 12. ($\mathbf{E}$) Quantitative analysis of the electric field intensity distribution along the Li anode surface and the corresponding tip electric field intensity under different dielectric constants varying from 4 to 12. ($\mathbf{F}$) Electric potential distribution in SEI under the case of the dielectric constant of the organic phase is 4 or 12. ($\mathbf{G}$) Local current density distribution of the B-Li and the LiF-FOM/Li. ($\mathbf{H}$) The morphology evolution of the Li on the B-Li and the LiF-FOM/Li during the deposition.

In stark contrast, because of the fluorine-dominated composition and its even distribution within the SEI of the LiF-FOM/Li, accelerated kinetics of Li⁺ flux with homogenized Li⁺ concentration distribution can be observed (Fig. 4G and fig. S27). The uniformly distributed Li⁺ flux would result in a homogeneous LCD on the LMA of the LiF-FOM/Li (Fig. 4G). Consequently, the following step of Li deposition on the LiF-FOM/Li anode would be flat and uniform as expected

than that on the B-Li one (Fig. 4H), which is in good agreement with the experimental observations (fig. S20). Moreover, uniform Li deposition induced by the LiF-FOM layer promotes more slight and uniform stress over the SEI (fig. S35), which prevents the fracture of the SEI during cycling. However, the rugged deposited Li on the B-Li is prone to concentrate the stress, which may lead to the fracture of the SEI as well as the Li dendrite to form dead Li during cycling.

Electrochemical performance of full cells

To evaluate the potential application and feasibility of the LiF-FOM protective layer in practical batteries, the LiF-FOM/Li anode (~10 mAh cm^{-2}) was paired with a LiFePO$_4$ (LFP) cathode (~2.3 mAh cm^{-2}) and LiNi$_{0.8}$Co$_{0.1}$Mn$_{0.1}$O$_2$ (NCM811) cathode (1.6 mAh cm^{-2}) to assemble full batteries using the ester-based electrolyte. Benefiting from efficient ion transport kinetics and interfacial stability of the LiF-FOM layer, the LFP||LiF-FOM/Li cell exhibited a high discharge capacity of ~134 mAh g^{-1} without obvious capacity decay with an average CE of 99.8% over 300 cycles (Fig. 5A and fig. S36). In contrast, the LFP||B-Li cell displayed a low capacity of 88.7 mAh g^{-1} after 150 cycles, followed by a rapid degradation of the capacity. Even at the high current density of 1 and 2 C, LFP||LiF-FOM/Li cells exhibit excellent cycling stability with higher capacity retention of 96.8 and 89.3% after 200 cycles, respectively (fig. S37). The advantage of

the LiF-FOM/Li anode was further exploited by coupling it with a high-voltage NCM811 cathode under lean electrolyte conditions. The NCM811||LiF-FOM/Li has much better rate capability and cyclability over the B-Li one (Fig. 5B), which delivers capacities of 194.5, 181.3, 147.1, and 101.4 mAh g^{-1} at a discharge rate of 0.3, 0.5, 1, and 2 C, respectively (Fig. 5C). When the discharge rate is switched back to 0.5 C, the capacity is back to 169.4 mAh g^{-1} (93.4% retention). Subsequently, the NMC811||LiF-FOM/Li full cell with lean electrolyte demonstrated a stable cycle of over 300 cycles with higher capacity retentions (60.2%) (Fig. 5, D and E). No considerable capacity drop and cell sudden death were observed during cycling, which is due to the LiF-FOM layer homogenizing the Li$^+$ flux, which, in turn, induces uniform Li deposition and minimizes the growth of tortuous Li dendrites. In contrast, the continuous formation of dendrites and dead Li on the B-Li anode and continuous consumption
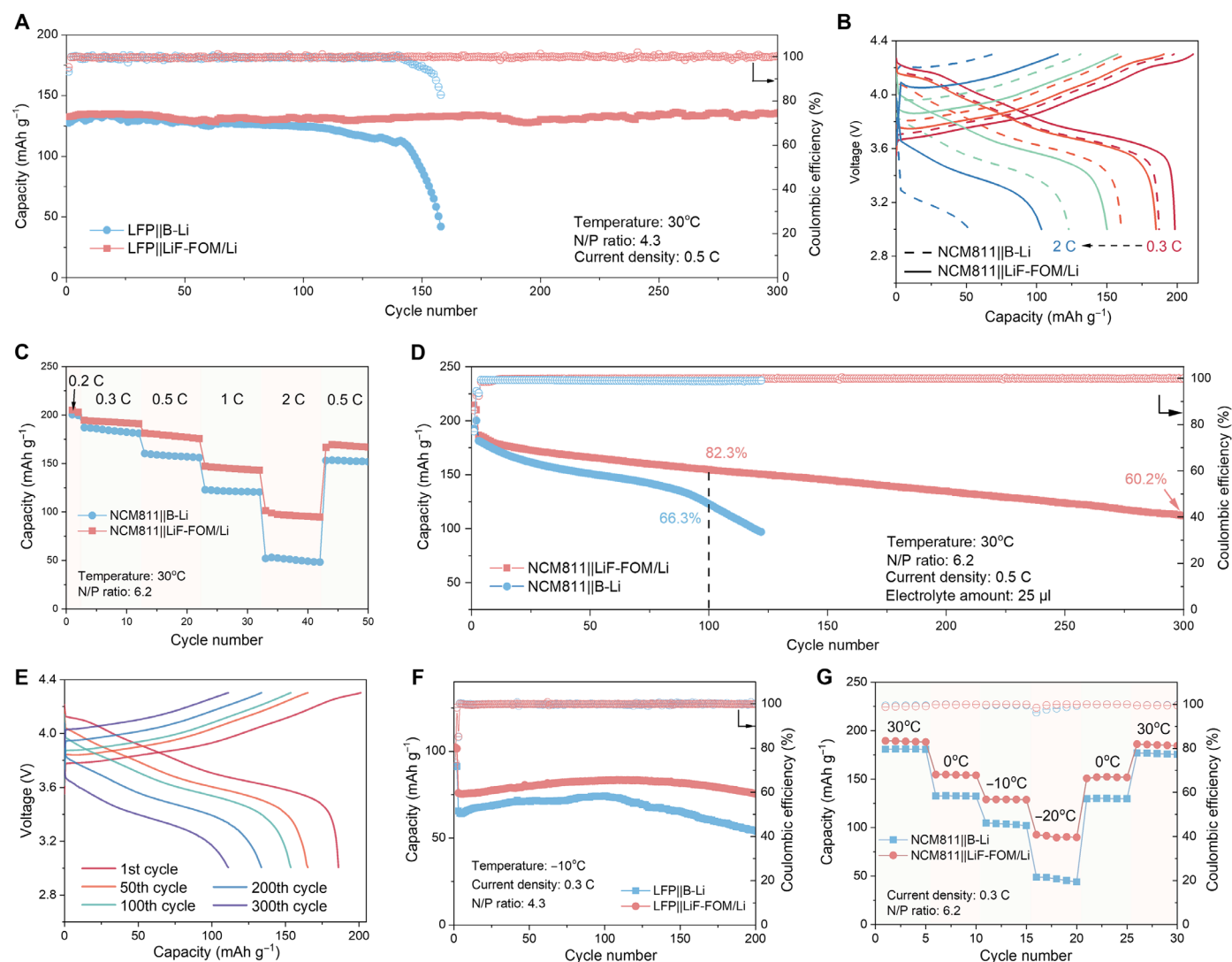

Fig. 5. Electrochemical performance of the full cells. (**A**) Discharge/charge voltage profiles of LFP||Li full cells with the B-Li and the LiF-FOM/Li anodes. (**B**) Discharge/charge voltage profiles of the NCM811||LiF-FOM/Li full cells at various current densities. (**C**) Rate capability of the NCM811||Li full cells with the B-Li and the LiF-FOM/Li anodes. (**D**) Cycling stability of NCM811||Li full cells with the B-Li and the LiF-FOM/Li anodes. (**E**) Discharge/charge voltage profiles of the NCM811||LiF-FOM/Li full cells after different cycles. (**F**) Cycling stability of LFP||Li full cells with the B-Li and the LiF-FOM/Li anodes at a low temperature of −10°C. (**G**) Discharge capacity of NCM811||Li full cells with the B-Li and the LiF-FOM/Li anodes at different temperatures.

of the limited electrolyte during the cycling would severely affect the Li$^+$ transport, leading to the abrupt reduction in the capacity of the NCM811||B-Li full cell for only 100 cycles (Fig. 5D). In addition, the NCM811||LiF-FOM/Li cell can achieve stabilization for 100 cycles with a capacity retention of 78.7% under extreme conditions of N/P = 2.5 and an area loading of 4 mAh cm^{-2}.

In addition to the excellent performance at room temperature, the ability to enable fast Li$^+$ transport of the LiF-FOM/Li makes the full cells working at low temperatures feasible. Compared with the LFP||B-Li full cell, the LFP||LiF-FOM/Li one shows a longer discharge plateau with a higher discharge capacity and lower potential hysteresis under different current densities at −10°C (fig. S39). Specifically, the LFP||LiF-FOM/Li delivers high capacities of 92.1, 82.5, 67.7, and 43.3 mAh g^{-1} at 0.2, 0.3, 0.5, and 1 C, respectively, and returned to 96.2 mAh g^{-1} at 0.3 C, indicating a high-rate capability with low voltage polarization. The specific discharge capacity is ~76.5 mAh g^{-1} cell at 0.3 C without capacity decay over 200 cycles at −10°C (Fig. 5F). By contrast, the LFP||B-Li cell faded rapidly over 120 cycles. Moreover, the NCM811||Li cells could also be operated stably over a wide temperature range (−20° to 30°C) (Fig. 5G). At −20°C, the discharge capacity of the NCM811||Li cell using the LiF-FOM/Li anode (~94 mAh g^{-1}) was almost two times that obtained with the B-Li one (~51 mAh g^{-1}), indicating excellent temperature tolerance and good stability of the LiF-FOM/Li anode over a wide temperature range.

DISCUSSION

In summary, we have successfully developed a high-voltage–engaged electrosynthesis strategy to construct a unique hybrid SEI with ultrahigh fluorine content on the LMA. Within this layer, ultrafine LiF nanocrystals and FOM can be formed abundantly and distributed homogeneously, whose high dielectric constants are found to promote a fast and uniform Li$^+$ transport via the organic-inorganic interface. In addition, the interfacial stability and mechanical strength of the SEI with such constituents can also be greatly improved. As a result, the LiF-FOM/Li anodes can deliver stable Li plating/stripping for more than 3600 or 1200 hours using ether-based electrolytes under the areal capacity and current density of 1 mAh cm^{-2} and 1 mA cm^{-2} or 5 mAh cm^{-2} and 5 mA cm^{-2}, respectively. The cell can exhibit long-term cycling even using corrosive ester-based electrolytes at high DOD. Stable cycling performance can also be achieved when paired such anodes with cathodes under lean electrolyte, low N/P ratio, and low-temperature conditions. This work may provide a special electrosynthetic protocol to create a functional organic-inorganic hybrid with a high dielectric constant, whose combination can effectively improve the ion transport properties that may find applications in advanced electrochemical systems.

MATERIALS AND METHODS
Materials
The pure Li foil (400 μm) and Li/Cu hybrid (50 μm) foil were bought from China Energy Lithium Co. Ltd. The LFP laminates (mass loading, ~13.5 mg cm^{-2}) were purchased from MTI Kejing Group. NCM811 cathodes with mass loading of ~8 and ~20 mg cm^{-2} were supplied by Guangdong Canrd New Energy Technology Co. Ltd. and also punched into 12-mm discs for use. The pure FEC and the ester-based and ether-based electrolytes were bought from Dodochem Group.

Synthesis of the LiF-FOM/Li
Pure lithium discs of 16-mm diameter and 400/50-μm thickness were used as both cathode and anode. The electrosynthesis experiments were realized in two electrode electrolytic cells. The FEC was used as an electrolyte for the electrosynthesis process. First, the FEC solvent is kept under high voltage (600 V) for 3 hours until a more stable Li$^+$-(FEC) solvation structure is formed. The cathode in the electrolytic cell was then replaced with fresh Li metal or Li/Cu hybrid foil, and electrodeposition was continued for 10 min at 600 V. Thereafter, the LiF-FOM layer was successfully obtained on Li metal. The synthetic process was stored in an Ar-filled glovebox.

Cell assembly and electrochemical measurement
CR2032-type coin cells were assembled in a glove box filled with Ar atmosphere (H$_2$O < 0.1 ppm, O$_2$ < 0.1 ppm). Neware multichannel battery test system (CT-4008) was used to evaluate the electrochemical performance. The Li symmetric cells were cycled at 1, 2, 3, or 5 mA cm^{-2} with a cycling capacity of 1 or 5 mAh cm^{-2}, respectively. The cells of Li-Li were tested in ester-based and ester-based electrolytes with different current densities and capacities, respectively. The ester-based electrolyte used in the Li symmetric cells experiment was 1.0 M LiPF$_6$ in ethylene carbonate/diethyl carbonate (EC/DEC) (1:1 in volume) without additive. The ester-based electrolyte was used for Li deposition morphology and SEI characterization after cycling. The ether-based electrolyte used in the Li symmetric cells experiment was 1.0 M lithium bis(trifluoromethane)sulfonimide in 1,3-dioxolane/1,2-dimethoxyethane (1:1 in volume) with 2% LiNO$_3$ as an additive. The t_{Li^+} was measured by applying a polarization voltage of 10 mV to Li||Li cells for 2 hours, and resistances before and after polarization were measured by EIS. Cyclic voltammetry (CV) measurements were tested in a Li symmetric cell with a scanning range from −0.2 to +0.2 V at a sweep rate of 1 mV s^{-1}. EIS was tested using Li||Li cells with 10-mV amplitude and frequency ranging from 10 mHz to 1 MHz. CV, Li$^+$ transference number, and EIS were tested on BioLogic SP-150 and CHI 760D electrochemical workstations. The full cells paired with LFP and NCM811 cathode were tested in ester electrolytes. The LFP/NCM811||Li full cells were assembled by using a B-Li or LiF-FOM/Li foil as the anode, a piece of Celgard 2500 separator, and an LFP/NCM811 cathode. It is noted that the electrolyte used in each cell was controlled as 40 μl except Li||NCM811 full cells using 25-μl electrolyte for lean electrolyte condition. The used B-Li or LiF-FOM/Li anode was prepared by a 50-μm Li/Cu hybrid electrode. The working potential window of the LFP||Li full cell was from 2.5 to 3.8 V. The working potential window of the NCM811||Li full cell was from 3 to 4.3 V. For galvanostatic charge/discharge tests over a wide temperature range from −20 to 30°C, a climatic chamber (Yiheng BPH-060B) was used. For low-temperature performance measurements, the cells were tested in 1.0 M LiPF$_6$ in EC/DEC (3:7 in volume) to lower the freezing point of the electrolyte. The diameter of all cathodes and anodes was 12 mm.

Material characterization
The morphology and microstructure of electrodes were studied using field emission SEM (FE-SEM; Nova Nano SEM 450). Attenuated total reflectance FTIR was carried out on an infrared spectrophotometer (Nicolet 6700). Raman spectroscopy was performed using a Renishaw via the Raman spectrometer system. ^{7}Li, ^{13}C, and ^{19}F NMR were performed on a Bruker AVANCE III 400 M at room temperature using CDCl$_3$ as a solvent. An AFM (MFP-3DSA) was

also used to investigate the surface morphology and Young's module of the electrode. MALDI-TOF-MS was performed on BRUKER Ultraflextreme using DHB to generate negative secondary ions. XPS (Thermo Scientific Nexsa) with a monochromatic Al-K_α x-ray source was performed to detect the chemistry of the sample. To avoid air exposure, the vacuum transfer vessel was used to transfer the samples. TOF-SIMS was performed by TOF-SIMS V (ION-TOF, TOF.SIMS 5-100, Germany) with 15 keV of Bi^{3+} primary ion beam. Two hundred fifty electron volts of Cs^+ ions was used to sputter the surface of Li to generate negative secondary ions. Depth profiles of secondary ions were collected by Cs^+ (250) on an area of 100×100 μm^2.

Cryo-TEM experiment

All cryo-TEM characterizations were performed on TEM (FEI Talos-S) operated at 200 kV with a Gatan 698 cryo-transfer holder. To prepare the LiF-FOM/Li sample, bare Cu mesh was pressed on Li foil, then moved to the high-voltage electrolytic cell working as a cathode under 600 V for 10 min. After that, the Cu mesh after LiF-FOM deposition was slightly removed from Li foil. Moreover, to characterize Li deposition behavior on B-Li and LiF-FOM/Li, the bare Cu mesh and LiF-FOM–deposited Cu mesh were placed on Li foil (Cu-mesh/Li) working as an anode assembled into a cell. The Li was first deposited on Cu-mesh/Li with an areal capacity of 0.5 mAh cm^{-2} at a current density of 0.5 mA cm^{-2} in the ester-based electrolyte. Subsequently, the samples were washed using DEC and dried. To characterize the composition and structure of LiF-FOM after cycling, we scraped off the SEI on the surface of the LiF-FOM/Li electrode after 500 cycles and dispersed it on the Cu mesh. All the Cu mesh was slightly transferred into the sealed container of the cryo-TEM holder in an Ar–filled glovebox. The cryo-TEM holder was quickly inserted into TEM, and the samples were kept stable by liquid nitrogen freezing at the low temperature of −180°C. All TEM images were taken at cryogenic temperature (−180°C).

Model building and AIMD simulations

In this study, all first-principles calculations were executed using the Vienna Ab Initio Simulation Package (54). The electron exchange and correlation energies were modeled using the Perdew-Burke-Ernzerhof functional within the framework of the generalized gradient approximation. Interactions between electrons and ions were addressed through projector-augmented wave pseudopotentials. We set the plane-wave basis expansion energy cutoff at 500 eV, complemented by a Gaussian smearing width of 0.1 eV. The Brillouin zone sampling was confined to the Γ-point. The criterion for convergence in our electronic structure calculations was a total energy variation below 10^{-4} eV within the self-consistent field method. We conducted AIMD simulations at 330 K in a $3 \times 3 \times 1$ supercell, under a canonical ensemble (NVT). Temperature fluctuations were regulated using a Nosé-Hoover thermostat. To facilitate a simulation time step of 1 fs (55), the mass of hydrogen in the system was replaced with that of tritium.

To accurately delineate the decomposition products of the electrolyte solvent on the lithium metal surface, a 1:1 volume ratio of EC/DEC, along with bare FEC, was studied. The LMA model was faceted using the (100) face, identified as the most stable crystallographic face of lithium. This faceted model was initially expanded to a 3×3 supercell, followed by the construction of a nine-layer atomic model. In this model, only the central three layers were fixed, allowing the top and bottom three layers to freely relax alongside the intermediary electrolyte, thereby adopting a conformation representative of the liquid phase. To mitigate the effects of periodic boundary conditions, a large cubic cell measuring $10 \times 10 \times 31$ Å was used and subjected to 20 ps of thermal equilibration. Within the simulation box, solvent molecules were introduced until the solvent's experimental density was achieved. The initial structure for each electrolyte system was configured on the basis of these densities, with FEC and Li added randomly in varying molar ratios. The radial distribution functions of Li-O and Li-F were derived from the final 15 ps of the AIMD trajectory for each system. Consequently, two characteristic products were identified to represent the components of the DEC-EC–derived organic matrix (OOM) (LiOCH$_2$CH$_2$OLi and CH$_3$CH$_2$OLi) and the FOM (CH$_2$CHOLi and CH$_2$CHOFOCOCO$_2$Li), as depicted in figs. S40 and S41.

Calculation of dielectric constant

To accurately simulate the environment of the decomposition products, our study used an implicit solvent model. This model necessitated a dielectric constant, which, in turn, required the calculation of dipole moments and volumes. To this end, classical MD simulations were carried out using the Large-scale Atomic/Molecular Massively Parallel Simulator (56). Subsequently, the Packing Optimization for Molecular Dynamics Simulations (PACKMOL) program (57) was used to construct simulation boxes for the organic decomposition products LiOCH$_2$CH$_2$OLi, CH$_2$CHOLi, CH$_3$CH$_2$OLi, and CH$_2$CHOFOCOCO$_2$Li, as detailed in figs. S40 and S41. The structural configurations of these products are presented in fig. S42. EC and DEC served as control groups throughout these simulations. In addition, the restrained electrostatic potential charges for the four lithium salts were determined using Gaussian 16 (58) and Multiwfn programs (59), facilitating their incorporation into the classical MD calculations.

The dielectric constant is calculated according to formula (1)

$$\varepsilon = \frac{<M^2> - <M>^2}{3\varepsilon_0 V K_B T} \tag{1}$$

where ε is the dielectric constant of the specific system, ε_0 is the dielectric constant of the vacuum, V is the volume of the simulation box, k is the Boltzmann constant, and T is the temperature. M is the total dipole moment of the system, and the dielectric constant data obtained from the above formulas are summarized in table S5.

Diffusion barriers calculation

The (111) surface of Li$_2$O and the (001) surface of LiF were selected and subsequently expanded into $2 \times 2 \times 2$ supercells, with a vacuum spacing of 20 Å intentionally created to eliminate potential interactions between the approximated surfaces. The diffusion barriers for Li$^+$ on Li$_2$O (111) and LiF (001) surfaces were then quantified using the CI-NEB method (60), with satisfactory energy convergence at 1×10^{-6} eV and force convergence at 0.02 eV Å^{-1}. This process culminated in the determination of the diffusion barriers for Li$^+$ on the surfaces of LiF and Li$_2$O inorganic compounds. It was observed that the diffusion resistance on the LiF surface was low, thus facilitating the diffusion of Li$^+$.

Diffusion coefficient calculations

In terms of the diffusion coefficient, it can be derived from the Arrhenius equation as shown

$$D = g\alpha^2 \nu \exp\left(\frac{E_a}{K_B T}\right) \quad (2)$$

where D denotes the diffusion coefficient, g refers to the dimensionality of diffusion, α signifies the migration distance of Li^+, ν symbolizes the lattice vibration frequency as approximated by crystal phonon calculations (with a standard frequency assumed at 10^{13} s^{-1}), E_a and K_B represent the activation energy and Boltzmann constant respectively, and T is the temperature.

Finite element analysis

A rectangular region with dimensions of 30 nm in length and 22 nm in width is constructed, where the upper part of this area corresponds to the SEI, whereas the lower part represents the uneven Li anode. Within the SEI, circular regions are used to symbolize the presence of randomly distributed inorganic phases, while the remaining regions represent the organic phase. Under static conditions, the intensity of the electric field is equal to the anode gradient of the potential

$$\mathbf{E} = -\nabla V \quad (3)$$

Combining this equation with the constitutive relationship of $\mathbf{D} = \varepsilon \varepsilon_0 \mathbf{E} + \mathbf{P}$ between the electric displacement $\mathbf{D}$ and the electric field $\mathbf{E}$ makes it possible to represent Gauss's law as the following equation

$$-\nabla \cdot (\varepsilon \varepsilon_0 \nabla V - \mathbf{P}) = \rho \quad (4)$$

where ε_0 and ε are the dielectric constant of vacuum and SEI, respectively, $\mathbf{P}$ is the electric polarization vector, and ρ is the space charge density.

The electrochemical and deposition behavior of Li^+ under the influence of two types of SEI was simulated using the COMSOL Multiphysics 6.0 platform. The main processes involved in the simulation include two major steps: charge transfer and Li^+ transport, and the following are control equations. The transport of Li^+ is caused by the migration driven by an electric field and diffusion induced by the concentration gradient, which can be described by the Nernst-Planck equation

$$N_i = -D_i \left(\nabla c_{0,i} - \frac{z_i F c_{0,i}}{RT}\nabla\Phi\right) \quad (5)$$

where N_i is flux, D_i, z_i, and $c_{0,i}$ are the diffusion coefficient, charge, and concentration of species i, respectively. F is the Faraday's constant, R is the ideal gas constant, T is the kelvin temperature, and Φ is the electrolyte potential. At the same time, Li^+ in the electrolyte adheres to the laws of charge conservation and mass conservation

$$\frac{\partial c_i}{\partial t} + \nabla \times N_i = 0 \quad (6)$$

$$\sum_i z_i c_i = 0 \quad (7)$$

where c_i is the concentration, and z_i is the valence of each species in the electrolyte.

During charging, at the anode interface, Li^+ is reduced to Li atom and deposited on the substrate surface. This process can be described by the following simplified equation

$$Li^+ + e^- \leftrightarrow Li \quad (8)$$

This process is controlled by the Butler-Volmer equation

$$i_{loc} = i_{ex}\left[\exp\left(\frac{\alpha_a F\eta}{RT}\right) - \exp\left(\frac{-\alpha_c F\eta}{RT}\right)\right] \quad (9)$$

where i_{loc} is the LCD, η is overpotential, α_a and α_c are the anodic and cathodic charge transfer coefficients, respectively, and i_{ex} is exchange current density.

The resulting deposition morphology was assumed to occur in the normal direction to the boundary with a velocity v_n

$$v_n = \frac{i_{loc}}{\mathbf{n}F}\frac{M}{\rho} \quad (10)$$

where M and ρ are the molar mass and density of Li metal, and $\mathbf{n}$ is the normal vector.

To construct the B-Li-SEI, we used a random function to describe the nonuniform distribution of SEI components as follows

$$f(x,y,z) = \sum_{m=-M}^{M}\sum_{n=-N}^{N}\sum_{h=-N}^{N}$$
$$\{a(m,n,h)\cos[2\pi(mx+ny+hz)+\varphi(m,n,h)]\} \quad (11)$$

where x, y, and z are the spatial coordinates, m, n, and h are the spatial frequencies, $a(m, n, h)$ is the amplitude, and $\varphi(m, n, h)$ is the phase angle. The amplitude is randomly generated by a Gaussian distribution function, and the phase angle and spatial frequency are derived from a uniform random distribution in a limited interval.

To construct the LiF-FOM/Li-SEI, we defined the following function to reflect the uniform and dense distribution of LiF nanocrystals

$$f(x,y,z) = \gamma$$
$$\{abs[\sin(10^4\pi x)] * abs[\sin(10^4\pi y)] * abs[\sin(10^4\pi z)] + \delta\} \quad (12)$$

where γ and δ are constants that could be used to adjust the size of the function.

For mechanical performance simulation, the displacement of the anode surface is calculated according to the above equations, and the kinematic stress-strain constitutive relation is given by Hooke's law

$$\sigma_{ij} = \frac{E}{1+\nu}\nabla\vec{\ell} + \frac{2\nu E}{1-2\nu} \quad (13)$$

where E is Young's modulus, $\vec{\ell}$ is the displacement of the Li-SEI interface, and ν is Poisson's ratio.

The simulation geometry and model are shown in the fig. S43. Both the anodic and cathodic charge transfer coefficients are set as 0.5, the exchange current density is set as 10 mA cm^{-2}, the Li^+ concentration in the electrolyte is set as 1 M, the temperature is fixed at 298 K, and the applied current density is 0.1 mA cm^{-2}. The diffusion coefficient of Li^+ varies from 10^{-9} to 10^{-13} m^2 s^{-1} in the SEI and Young's modulus range of SEI is set to 6 to 0.1 GPa and is consistent with the diffusion coefficient distribution.

Supplementary Materials

This PDF file includes:
Figs. S1 to S43
Tables S1 to S5
References

REFERENCES AND NOTES

1. C. Sanchez, P. Belleville, M. Popalld, L. Nicole, Applications of advanced hybrid organic-inorganic nanomaterials: From laboratory to market. *Chem. Soc. Rev.* **40**, 696–753 (2011).

2. T. M. Brenner, D. A. Egger, L. Kronik, G. Hodes, D. Cahen, Hybrid organic—inorganic perovskites: Low-cost semiconductors with intriguing charge-transport properties. *Nat. Rev. Mater.* **1**, 15007 (2016).

3. A. P. Wight, M. E. Davis, Design and preparation of organic-inorganic hybrid catalysts. *Chem. Rev.* **102**, 3589–3614 (2022).

4. Y. Gao, Z. Yan, J. L. Gray, X. He, D. Wang, T. Chen, Q. Huang, Y. C. Li, H. Wang, S. H. Kim, T. E. Mallouk, D. Wang, Polymer-inorganic solid-electrolyte interphase for stable lithium metal batteries under lean electrolyte conditions. *Nat. Mater.* **18**, 384–389 (2019).

5. A. C. Balazs, T. Emrick, T. P. Russell, Nanoparticle polymer composites: Where two small worlds meet. *Science* **314**, 1107–1110 (2006).

6. X. Xu, Z. Lou, S. Cheng, P. C. Y. Chow, N. Koch, H.-M. Cheng, Van der Waals organic/inorganic heterostructures in the two-dimensional limit. *Chem* **7**, 2989–3026 (2021).

7. C. Sanchez, B. Julián, P. Belleville, M. Popall, Applications of hybrid organic–inorganic nanocomposites. *J. Mater. Chem.* **15**, 3559–3592 (2005).

8. P. Calado, A. M. Telford, D. Bryant, X. Li, J. Nelson, B. C. O'Regan, P. R. F. Barnes, Evidence for ion migration in hybrid perovskite solar cells with minimal hysteresis. *Nat. Commun.* **7**, 13831 (2016).

9. F. Ye, S. Zhang, J. Warby, J. Wu, E. Gutierrez-Partida, F. Lang, S. Shah, E. Saglamkaya, B. Sun, F. Zu, S. Shoaee, H. Wang, B. Stiller, D. Neher, W.-H. Zhu, M. Stolterfoht, Y. Wu, Overcoming C_{60}-induced interfacial recombination in inverted perovskite solar cells by electron-transporting carborane. *Nat. Commun.* **13**, 7454 (2022).

10. S. Peng, J. Ma, P. Li, S. Zang, Y. Zhang, Y. Song, Regulation of quantum wells width distribution in 2D perovskite films for photovoltaic application. *Adv. Funct. Mater.* **32**, 2205289 (2022).

11. R. Femmer, A. Mani, M. Wessling, Ion transport through electrolyte/polyelectrolyte multi-layers. *Sci. Rep.* **5**, 11583 (2015).

12. W. Al Zoubi, M. P. Kamil, S. Fatimah, N. Nashrah, Y. G. Ko, Recent advances in hybrid organic-inorganic materials with spatial architecture for state-of-the-art applications. *Prog. Mater. Sci.* **112**, 100663 (2020).

13. X. B. Cheng, R. Zhang, C. Z. Zhao, Q. Zhang, Toward safe lithium metal anode in rechargeable batteries: A review. *Chem. Rev.* **117**, 10403–10473 (2017).

14. G. Lu, J. Nai, D. Luan, X. Tao, X. W. Lou, Surface engineering toward stable lithium metal anodes. *Sci. Adv.* **9**, eadf1550 (2023).

15. Y. Li, W. Huang, Y. Li, A. Pei, D. T. Boyle, Y. Cui, Correlating structure and function of battery interphases at atomic resolution using cryoelectron microscopy. *Joule* **2**, 2167–2177 (2018).

16. H. Yuan, J. Zheng, G. Lu, L. Zhang, T. Yan, J. Luo, Y. Wang, Y. Liu, T. Guo, Z. Wang, J. Nai, X. Tao, Formation of 2D amorphous lithium sulfide enabled by Mo_2C clusters loaded carbon scaffold for high-performance lithium sulfur batteries. *Adv. Mater.* **38**, 2400639 (2024).

17. P. C. Zou, H. Zhan, C. Wang, H. L. Xin, H. M. Cheng, F. Kang, C. Yang, Polymorph evolution mechanisms and regulation strategies of lithium metal anode under multiphysical fields. *Chem. Rev.* **121**, 5986–6056 (2021).

18. Y. Wang, Z. Wu, F. M. Azad, Y. Zhu, L. Wang, C. J. Hawker, A. K. Whittaker, M. Forsyth, C. Zhang, Fluorination in advanced battery design. *Nat. Rev. Mater.* **9**, 119–133 (2024).

19. J. Zhao, L. Liao, F. Shi, T. Lei, G. Chen, A. Pei, J. Sun, K. Yan, G. Zhou, J. Xie, C. Liu, Y. Li, Z. Liang, Z. Bao, Y. Cui, Surface fluorination of reactive battery anode materials for enhanced stability. *J. Am. Chem. Soc.* **139**, 11550–11558 (2017).

20. A. Hu, W. Chen, X. Du, Y. Hu, T. Lei, H. Wang, L. Xue, Y. Li, H. Sun, Y. Yan, J. Long, C. Shu, J. Zhu, B. Li, X. Wang, J. Xiong, An artificial hybrid interphase for an ultrahigh-rate and practical lithium metal anode. *Energ. Environ. Sci.* **14**, 4115–4124 (2021).

21. X. L. Fan, X. Ji, F. D. Han, J. Yue, J. Chen, L. Chen, T. Deng, J. Jiang, C. S. Wang, Fluorinated solid electrolyte interphase enables highly reversible solid-state Li metal battery. *Sci. Adv.* **4**, eaau9245 (2018).

22. J. Tan, J. Matz, P. Dong, J. Shen, M. Ye, A growing appreciation for the role of LiF in the solid electrolyte interphase. *Adv. Energy Mater.* **11**, 2100046 (2021).

23. Y.-H. Tan, G.-X. Lu, J.-H. Zheng, F. Zhou, M. Chen, T. Ma, L.-L. Lu, Y.-H. Song, Y. Guan, J. Wang, Z. Liang, W.-S. Xu, Y. Zhang, X. Y. Tao, H.-B. Yao, Lithium fluoride in electrolyte for stable and safe lithium-metal batteries. *Adv. Mater.* **33**, e2102134 (2021).

24. H. Zhang, G. G. Eshetu, X. Judez, C. Li, L. M. Rodriguez-Martinez, M. Armand, Electrolyte additives for lithium metal anodes and rechargeable lithium metal batteries: Progress and perspectives. *Angew. Chem. Int. Ed.* **57**, 15002–15027 (2018).

25. J. Wang, Y. Yamada, K. Sodeyama, C. H. Chiang, Y. Tateyama, A. Yamada, Superconcentrated electrolytes for a high-voltage lithium-ion battery. *Nat. Commun.* **7**, 12032 (2016).

26. X. Peng, T. Wang, B. Liu, Y. Li, T. Zhao, A solvent molecule reconstruction strategy enabling a high-voltage ether-based electrolyte. *Energ. Environ. Sci.* **15**, 5350–5361 (2022).

27. Y. J. Liu, X. Y. Tao, Y. Wang, C. Jiang, C. Ma, O. W. Sheng, G. X. Lu, X. W. Lou, Self-assembled monolayers direct a LiF-rich interphase toward long-life lithium metal batteries. *Science* **375**, 739–745 (2022).

28. Z. Ju, C. Jin, X. Cai, O. Sheng, J. Wang, J. Luo, H. Yuan, G. Lu, X. Tao, Z. Liang, Cationic interfacial layer toward a LiF-enriched interphase for stable Li metal batteries. *ACS Energy Lett.* **8**, 486–493 (2022).

29. Z. Cao, X. Zheng, M. Zhou, T. Zhao, L. Lv, Y. Li, Z. Wang, W. Luo, H. Zheng, Electrolyte solvation engineering toward high-rate and low-temperature silicon-based batteries. *ACS Energy Lett.* **7**, 3581–3592 (2022).

30. G. Park, K. K. Lee, D.-J. Yoo, J. W. Choi, Strategy for stable interface in lithium metal batteries: Free solvent derived vs anion derived. *ACS Energy Lett.* **7**, 4274–4281 (2022).

31. M. Mao, X. Ji, Q. Wang, Z. Lin, M. Li, T. Liu, C. Wang, Y. S. Hu, H. Li, X. Huang, L. Chen, L. Suo, Anion-enrichment interface enables high-voltage anode-free lithium metal batteries. *Nat. Commun.* **14**, 1082 (2023).

32. Z. Piao, H. R. Ren, G. Lu, K. Jia, J. Tan, X. Wu, Z. Zhuang, Z. Han, C. Li, R. Gao, X. Tao, G. Zhou, H. M. Cheng, Stable operation of lithium metal batteries with aggressive cathode chemistries at 4.9 V. *Angew. Chem. Int. Ed.* **62**, e202300966 (2023).

33. D. O'Hagan, Understanding organofluorine chemistry. An introduction to the C-F bond. *Chem. Soc. Rev.* **37**, 308–319 (2008).

34. J. Xie, S. Y. Sun, X. Chen, L. P. Hou, B. Q. Li, H. J. Peng, J. Q. Huang, X. Q. Zhang, Q. Zhang, Fluorinating the solid electrolyte interphase by rational molecular design for practical lithium-metal batteries. *Angew. Chem. Int. Ed.* **61**, e202204776 (2022).

35. Y. Kamikawa, K. Amezawa, K. Terada, Energy-loss near-edge structures and low-loss structures of polymers in a solid electrolyte interface formed from fluoroethylene carbonate on a Si anode clarified by DFT calculations. *J. Phys. Chem. C* **125**, 3890–3900 (2021).

36. E. Markevich, G. Salitra, D. Aurbach, Fluoroethylene carbonate as an important component for the formation of an effective solid electrolyte interphase on anodes and cathodes for advanced Li-ion batteries. *ACS Energy Lett.* **2**, 1337–1345 (2017).

37. L. Zhang, T. Yang, C. Du, Q. Liu, Y. Tang, J. Zhao, B. Wang, T. Chen, Y. Sun, P. Jia, H. Li, L. Geng, J. Chen, H. Ye, Z. Wang, Y. Li, H. Sun, X. Li, Q. Dai, Y. Tang, Q. Peng, T. Shen, S. Zhang, T. Zhu, J. Huang, Lithium whisker growth and stress generation in an in situ atomic force microscope-environmental transmission electron microscope set-up. *Nat. Nanotechnol.* **15**, 94–98 (2020).

38. Z. Ju, G. Lu, O. Sheng, H. Yuan, S. Zhou, T. Liu, Y. Liu, Y. Wang, J. Nai, W. Zhang, X. Tao, Soybean protein fiber enabled controllable Li deposition and a LiF-nanocrystal-enriched interface for stable Li metal batteries. *Nano Lett.* **22**, 1374–1381 (2022).

39. E. Markevich, G. Salitra, F. Chesneau, M. Schmidt, D. Aurbach, Very stable lithium metal stripping-plating at a high rate and high areal capacity in fluoroethylene carbonate-based organic electrolyte solution. *ACS Energy Lett.* **2**, 1321–1326 (2017).

40. X.-B. Cheng, C. Yan, X. Chen, C. Guan, J.-Q. Huang, H.-J. Peng, R. Zhang, S.-T. Yang, Q. Zhang, Implantable solid electrolyte interphase in lithium-metal batteries. *Chem* **2**, 258–270 (2017).

41. X. He, D. Bresser, S. Passerini, F. Baakes, U. Krewer, J. Lopez, C. T. Mallia, Y. Shao-Horn, I. Cekic-Laskovic, S. Wiemers-Meyer, F. A. Soto, V. Ponce, J. M. Seminario, P. B. Balbuena, H. Jia, W. Xu, Y. Xu, C. Wang, B. Horstmann, R. Amine, C. Su, J. Shi, K. Amine, M. Winter, A. Latz, R. Kostecki, The passivity of lithium electrodes in liquid electrolytes for secondary batteries. *Nat. Rev. Mater.* **6**, 1036–1052 (2021).

42. Y. Wang, F. Liu, G. Fan, X. Qiu, J. Liu, Z. Yan, K. Zhang, F. Cheng, J. Chen, Electroless formation of a fluorinated Li/Na hybrid interphase for robust lithium anodes. *J. Am. Chem. Soc.* **143**, 2829–2837 (2021).

43. S. Li, J. Huang, Y. Cui, S. Liu, Z. Chen, W. Huang, C. Li, R. Liu, R. Fu, D. Wu, A robust all-organic protective layer towards ultrahigh-rate and large-capacity Li metal anodes. *Nat. Nanotechnol.* **17**, 613–621 (2022).

44. X. Shen, Y. Li, T. Qian, J. Liu, J. Zhou, C. Yan, J. B. Goodenough, Lithium anode stable in air for low-cost fabrication of a dendrite-free lithium battery. *Nat. Commun.* **10**, 900 (2019).

45. Y. Xie, Y. Huang, Y. Zhang, T. Wu, S. Liu, M. Sun, B. Lee, Z. Lin, H. Chen, P. Dai, Z. Huang, J. Yang, C. Shi, D. Wu, L. Huang, Y. Hua, C. Wang, S. Sun, Surface modification using heptafluorobutyric acid to produce highly stable Li metal anodes. *Nat. Commun.* **14**, 2883 (2023).

46. C. B. Jin, T. F. Liu, O. W. Sheng, M. Li, W. K. Zhang, J. W. Nai, Z. J. Ju, Y. J. Liu, T. C. Liu, Y. Wang, Y. F. Yuan, Z. Lin, J. Lu, X. Y. Tao, Rejuvenating dead lithium supply in lithium metal anodes by iodine redox. *Nat. Energy* **6**, 378–387 (2021).

47. M. H. Kim, T. U. Wi, J. Seo, A. Choi, S. Ko, J. Kim, U. Jung, M. S. Kim, C. Park, S. Jin, H. W. Lee, Design principles for fluorinated interphase evolution via conversion-type alloying processes for anticorrosive lithium metal anodes. *Nano Lett.* **23**, 3582–3591 (2023).

48. W. Huang, H. Wang, D. T. Boyle, Y. Li, Y. Cui, Resolving nanoscopic and mesoscopic heterogeneity of fluorinated species in battery solid-electrolyte interphases by cryogenic electron microscopy. *ACS Energy Lett.* **5**, 1128–1135 (2020).

49. J. Zheng, Z. Ju, B. Zhang, J. Nai, T. Liu, Y. Liu, Q. Xie, W. Zhang, Y. Wang, X. Tao, Lithium ion diffusion mechanism on the inorganic components of the solid-electrolyte interphase. *J. Mater. Chem. A* **9**, 10251–10259 (2021).

50. W. Zhou, J. Gu, Z. Yang, M. Wang, Q. Zhao, Basis and effects of ion migration on photovoltaic performance of perovskite solar cells. *J. Phys. D Appl. Phys.* **54**, 063001 (2020).

51. N. Salles, L. Martin-Samos, S. de Gironcoli, L. Giacomazzi, M. Valant, A. Hemeryck, P. Blaise, B. Sklenard, N. Richard, Collective dipole effects in ionic transport under electric fields. *Nat. Commun.* **11**, 3330 (2020).

52. J. F. Liu, Z. Y. Wu, F. J. Stadler, Y. F. Huang, High dielectric poly(vinylidene fluoride)-based polymer enables uniform lithium-ion transport in solid-state ionogel electrolytes. *Angew. Chem. Int. Ed.* **62**, e202300243 (2023).

53. O. Tamwattana, H. Park, J. Kim, I. Hwang, G. Yoon, T.-H. Hwang, Y.-S. Kang, J. Park, N. Meethong, K. Kang, High-dielectric polymer coating for uniform lithium deposition in anode-free lithium batteries. *ACS Energy Lett.* **6**, 4416–4425 (2021).

54. G. Kresse, J. Furthmüller, Efficiency of ab-initio total energy calculations for metals and semiconductors using a plane-wave basis set. *Comp. Mater. Sci.* **6**, 15–50 (1996).

55. I. M. Markus, G. Jones, J. M. García, Investigation of electrolyte concentration effects on the performance of lithium-oxygen batteries. *J. Phy. Chem. C* **120**, 5949–5957 (2016).

56. M. Parrinello, A. Rahman, Polymorphic transitions in single crystals: A new molecular dynamics method. *J. Appl. Phy.* **52**, 7182–7190 (1981).

57. L. Martínez, R. Andrade, E. G. Birgin, J. M. Martínez, PACKMOL: A package for building initial configurations for molecular dynamics simulations. *J. Comput. Chem.* **30**, 2157–2164 (2009).

58. A. D. Becke, Density-functional thermochemistry. III. The role of exact exchange. *J. Chem. Phy.* **98**, 5648–5652 (1993).

59. T. Lu, F. Chen, Multiwfn: A multifunctional wavefunction analyzer. *J. Comput. Chem.* **33**, 580–592 (2012).

60. G. Henkelman, B. P. Uberuaga, H. Jónsson, A climbing image nudged elastic band method for finding saddle points and minimum energy paths. *J. Chem. Phy.* **113**, 9901–9904 (2000).

61. H. Kwon, H. Kim, J. Hwang, W. Oh, Y. Roh, D. Shin, H.-T. Kim, Borate–pyran lean electrolyte-based Li-metal batteries with minimal Li corrosion. *Nat. Energy* **9**, 57–69 (2024).

62. S. Weng, X. Zhang, G. Yang, S. Zhang, B. Ma, Q. Liu, Y. Liu, C. Peng, H. Chen, H. Yu, X. Fan, T. Cheng, L. Chen, Y. Li, Z. Wang, X. Wang, Temperature-dependent interphase formation and Li$^+$ transport in lithium metal batteries. *Nat. Commun.* **14**, 4474 (2023).

63. Y. Yin, Y. Yang, D. Cheng, M. Mayer, J. Holoubek, W. Li, G. Raghavendran, A. Liu, B. Lu, D. M. Davies, Z. Chen, O. Borodin, Y. S. Meng, Fire-extinguishing, recyclable liquefied gas electrolytes for temperature-resilient lithium-metal batteries. *Nat. Energy* **7**, 548–559 (2022).

64. R. Deng, F. Chu, F. Kwofie, Z. Guan, J. Chen, F. Wu, A low-concentration electrolyte for high-voltage lithium-metal batteries: Fluorinated solvation shell and low salt concentration effect. *Angew. Chem. Int. Ed.* **61**, e202215866 (2022).

65. M. Chen, J. H. Zheng, Y. J. Liu, O. W. Sheng, Z. J. Ju, G. X. Lu, T. F. Liu, Y. Wang, J. W. Nai, Q. Wang, X. Y. Tao, Marrying ester group with lithium salt: Cellulose-acetate-enabled LiF-enriched interface for stable lithium metal anodes. *Adv. Funct. Mater.* **31**, 2102228 (2021).

66. S. Cao, X. He, L. Nie, J. Hu, M. Chen, Y. Han, K. Wang, K. Jiang, M. Zhou, CF$_4$ plasma-generated plasma-generated LiF-Li$_2$C$_2$ artificial layers for dendrite-free lithium-metal anodes. *Adv. Sci.* **9**, e2201147 (2022).

67. W. W. Wang, Y. Gu, H. Yan, S. Li, J.-W. He, H.-Y. Xu, Q.-H. Wu, J.-W. Yan, B.-W. Mao, Evaluating solid-electrolyte interphases for lithium and lithium-free anodes from nanoindentation features. *Chem* **6**, 2728–2745 (2020).

68. C. Luo, H. Hu, T. Zhang, S. Wen, R. Wang, Y. An, S. S. Chi, J. Wang, C. Wang, J. Chang, Z. Zheng, Y. Deng, Roll-to-roll fabrication of zero-volume-expansion lithium-composite anodes to realize high-energy-density flexible and stable lithium-metal batteries. *Adv. Mater.* **34**, e2205677 (2022).

69. H. D. Yuan, J. W. Nai, H. Tian, Z. J. Ju, W. K. Zhang, Y. J. Liu, X. Y. Tao, X. W. Lou, An ultrastable lithium metal anode enabled by designed metal fluoride spansules. *Sci. Adv.* **6**, eaaz3112 (2020).

70. H. J. Liu, C. Y. Yang, M. C. Han, C. Y. Yu, X. Li, Z. Z. Yu, J. Qu, In-situ constructing a heterogeneous layer on lithium metal anodes for dendrite-free lithium deposition and high Li-ion flux. *Angew. Chem. Int. Ed.* **62**, e202217458 (2023).

71. Z. Luo, S. Li, L. Yang, Y. Tian, L. Xu, G. Zou, H. Hou, W. Wei, L. Chen, X. Ji, Interfacially redistributed charge for robust lithium metal anode. *Nano Energy* **87**, 106212 (2021).

72. Z. Han, H. R. Ren, Z. Huang, Y. Zhang, S. Gu, C. Zhang, W. Liu, J. Yang, G. Zhou, Q. H. Yang, W. Lv, A permselective coating protects lithium anode toward a practical lithium-sulfur battery. *ACS Nano* **17**, 4453–4462 (2023).

73. H. Zhang, Y. Wang, S. Ju, P. Gao, T. Zou, T. Zhang, J. Wang, G. Xia, X. Yu, 3D artificial electron and ion conductive pathway enabled by MgH$_2$ nanoparticles supported on g-C$_3$N$_4$ towards dendrite-free Li metal anode. *Energy Storage Mater.* **52**, 220–229 (2022).

74. Z. Guo, Q. Zhang, C. Wang, Y. Zhang, S. Dong, G. Cui, I-containing polymer/alloy layer-based Li anode mediating high-performance lithium–air batteries. *Adv. Funct. Mater.* **32**, 2108993 (2021).

75. G. Lu, J. Nai, H. Yuan, J. Wang, J. Zheng, Z. Ju, C. Jin, Y. Wang, T. Liu, Y. Liu, X. Tao, In-situ electrodeposition of nanostructured carbon strengthened interface for stabilizing lithium metal anode. *ACS Nano* **16**, 9883–9893 (2022).

76. M. Shang, O. G. Shovon, F. E. Y. Wong, J. Niu, A BF$_3$-doped MXene dual-layer interphase for a reliable lithium-metal anode. *Adv. Mater.* **35**, e2210111 (2023).

77. X. Li, Y. Tian, L. Shen, Z. Qu, T. Ma, F. Sun, X. Liu, C. Zhang, J. Shen, X. Li, L. Gao, S. Xiao, T. Liu, Y. Liu, Y. F. Lu, Electrolyte interphase built from anionic covalent organic frameworks for lithium dendrite suppression. *Adv. Funct. Mater.* **31**, 2009718 (2021).

78. C. Wei, L. Tan, Y. Tao, Y. An, Y. Tian, H. Jiang, J. Feng, Y. Qian, Interfacial passivation by room-temperature liquid metal enabling stable 5 V-class lithium-metal batteries in commercial carbonate-based electrolyte. *Energy Storage Mater.* **34**, 12–21 (2021).

79. Y. L. Cui, S. F. Liu, D. H. Wang, X. L. Wang, X. H. Xia, C. D. Gu, J. P. Tu, A facile way to construct stable and ionic conductive lithium sulfide nanoparticles composed solid electrolyte interphase on Li metal anode. *Adv. Funct. Mater.* **31**, 2006380 (2020).

80. Q. Xu, J. Lin, C. Ye, X. Jin, D. Ye, Y. Lu, G. Zhou, Y. Qiu, W. Li, Air-stable and dendrite-free lithium metal anodes enabled by a hybrid interphase of C$_{60}$ and Mg. *Adv. Energy Mater.* **10**, 1903292 (2019).

81. T. Chen, F. Meng, Z. Zhang, J. Liang, Y. Hu, W. Kong, X. L. Zhang, Z. Jin, Stabilizing lithium metal anode by molecular beam epitaxy grown uniform and ultrathin bismuth film. *Nano Energy* **76**, 105068 (2020).

82. F. Liu, L. Wang, Z. Zhang, P. Shi, Y. Feng, Y. Yao, S. Ye, H. Wang, X. Wu, Y. Yu, A mixed lithium-ion conductive Li$_2$S/Li$_2$Se protection layer for stable lithium metal anode. *Adv. Funct. Mater.* **30**, 2001607 (2020).

83. D. C. Lin, Y. Y. Liu, W. Chen, G. M. Zhou, K. Liu, B. Dunn, Y. Cui, Conformal lithium fluoride protection layer on three-dimensional lithium by nonhazardous gaseous reagent freon. *Nano Lett.* **17**, 3731–3737 (2017).

84. G. Li, X. Duan, X. Liu, R. Zhan, X. Wang, J. Du, Z. Chen, Y. Li, Z. Cai, Y. Shen, Y. Sun, Locking active Li metal through localized redistribution of fluoride enabling stable Li-metal batteries. *Adv. Mater.* **35**, e2207310 (2023).

85. R. M. Gao, H. Yang, C. Y. Wang, H. Ye, F. F. Cao, Z. P. Guo, Fatigue-resistant interfacial layer for safe lithium metal batteries. *Angew. Chem. Int. Ed.* **60**, 25508–25513 (2021).

86. A. Jain, S. P. Ong, G. Hautier, W. Chen, W. D. Richards, S. Dacek, S. Cholia, D. Gunter, D. Skinner, G. Ceder, K. A. Persson, Commentary: The materials project: A materials genome approach to accelerating materials innovation. *APL Mater.* **1**, 011002 (2013).